Inlet Gap Effect on Aerodynamics and Tonal Noise Generation of a Voluteless Centrifugal Fan

(article starts on next page)

Inlet gap effect on aerodynamics and tonal noise generation of a voluteless centrifugal fan

M. Ottersten [a,b,*], H.D. Yao [a], L. Davidson [a]

[a] *Department of Mechanics and Maritime Science, Chalmers University of Technology, Gothenburg, Sweden*
[b] *Swegon Operation, Box 336, Gothenburg SE-401 25, Sweden*

ARTICLE INFO

ABSTRACT

In this paper, the gap effects on the aerodynamics and tonal noise generation of voluteless centrifugal fans are studied based on different gap geometries. The study is motivated by the state of the art of this type of fan, for which the tonal noise generation due to the gap turbulence has not been addressed concerning the gap geometry, while a recent study reported that there is tonal noise at the blade passing frequency (BPF) from the gap turbulence. We simulate the configurations using a hybrid method coupling the improved delayed detached eddy simulation (IDDES) with Formulation 1A of Farassat. Our simulation shows regions with high vorticity magnitudes in the channel between two blades near the trailing edges close to the shroud. The turbulence renders a uniform pressure rise. By changing the gap design, the turbulent regions can be reduced. The configurations show a similar trend of the root mean square (RMS) pressure on the blade leading edge (BLE), largest at the shroud, and decays when the distance to the gap increases. The gap designs affect the amplitude of the RMS pressure, which is connected to the BPF. Spectral analysis is performed for the surface pressure fluctuations and the sound pressure upstream of the fan. The surface pressure fluctuations show that, for all cases, the regions with high energy are identical to the locations where the gap turbulence evolves and accounts for the impingement on the BLE. The amplitude of the tonal noise at the BPF differs between the cases.

1. Introduction

Today most people spend the majority of their time indoors. The indoor environmental quality (IEQ) has become more and more important. When considering IEQ we usually think about temperature, CO_2 level, and humidity. However, it has been established that noise pollution is also an important factor affecting IEQ [1,2], because the noise is harmful to human's health not only by directly causing loss of hearing and tinnitus but also by indirectly producing annoyance, sleep disturbance, and stress [3,4].

The structure of modern buildings is good at reducing external noise from traffic, and significant improvements have been made over recent years [5]. Although the internal noise from heating, ventilation, and air conditioning (HVAC) systems is difficult to isolate, low-speed centrifugal fans installed in the HVAC systems are known as dominant noise contributors. The frequency of the tonal noise is connected to the rotation speed of the fan. In variable air volume (VAV) systems the fan speed changes continuously to meet the demand. It means that the tonal noise changes continuously over a wide range of frequencies. The noise can be reduced by placing silencers in ducts, but the silencers introduce additional pressure loss. Besides, the silencers are mainly effective in absorbing
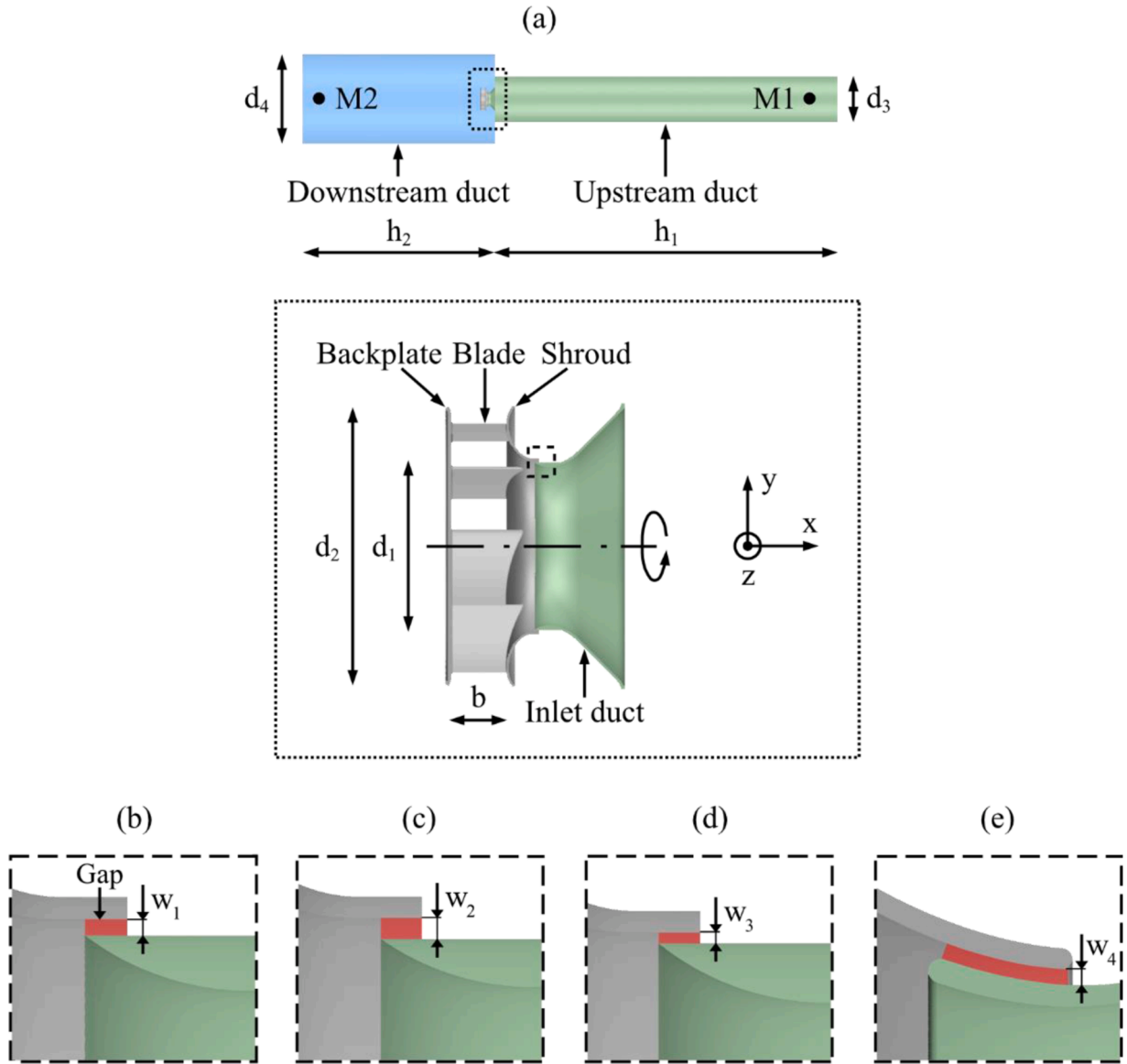

Fig. 1. The fan configurations. Gray indicates the rotating fan and green the stationary inlet duct. The gap location is marked out with red zone. (a) the simple geometry layout for the numerical simulation. (b) Case 1 (baseline), (c) Case 2 (larger gap width), (d) Case 3 (smaller gap width), and (e) Case 4 (curved gap, same gap width).

broadband noise rather than tonal noise. They can be tuned to damp the tonal noise at specific frequencies, while the tuning is not valid for a wide range of frequencies [6].

Nowadays a ventilation system is usually driven by voluteless centrifugal fans. These are fans where the volute (spiral casing surrounding the fan) is removed, termed voluteless in this study. The reason for choosing voluteless fans is that the removal of the volutes can reduce flow losses to achieve efficient aerodynamic performance and lower noise levels. Regarding the structure of the rotor part, a front shroud and a backplate are assembled onto the top and bottom sides of the rotating blades, respectively. The fan tonal noise generation is attributed to multiple causes. Pressure and density fluctuations on fan blades are identified as dominant sources in a large body of studies, e.g., by Ffowcs Williams and Hawkings [7]. As found in both simulations and experiments for voluteless fans [8], the tonal noise at the blade passing frequency (*BPF*) is generated from a helical unsteady inlet vortex that interacts with the rotating blades near the fan backplate. Another cause is inflow distortion, which leads to flow separation at the blade root near the backplate [9]. Based on this finding, flow obstructions were proposed upstream of the fan inlet [10]. The shape and location of the obstructions were identified as the key parameters for noise reduction. As the present study focuses on tonal noise, broadband noise sources (e.g., see Ref. [11]) are not reviewed.

In an HVAC voluteless centrifugal fan, there is a gap (also termed clearance) between the rotating fan front shroud and the

Table 1
The fan parameters.

d_1	d_2	d_3	d_4	b	h_1	h_2
0.165 m	0.268 m	0.6 m	1.1 m	0.053 m	4.0 m	2.3 m

Table 2
The gap width.

w_1	w_2	w_3	w_4
1.5 mm	2.0 mm	1.0 mm	1.5 mm

stationary inlet duct, see Fig. 1. The pressure difference between the fan's inner and outer sides drives air to pass through the gap. As clarified by Hariharan and Govardhan [12], increasing the gap width worsens the blade aerodynamic performance. According to Lee [13], the gap gives rise to a local jet that aggravates flow separation near the front shroud. This finding was further proven in later studies [14,15], where the visualization of streamlines indicates that the flow discharged from the gap creates recirculating flow around the intersection of the front shroud and the blade trailing edge. The flow separation features intensive turbulence kinetic energy (TKE) [15]. As demonstrated in experiments [16,17], the curved shape of the front shroud also accounts for the flow separation. It is worth noting that the shroud skin friction leads to extra rotational momentum near the shroud walls. The same finding was also reported in [18]. This effect is different from conventional blade vortex interaction (e.g., [19]), where the flow upstream of the blades is quiescent.

The noise from voluteless centrifugal fans was numerically studied by Schaefer and Boehle [20]. It was found that the accuracy of the noise prediction, especially at *BPF*, is improved when the mesh is refined at the gap and the fan outlet. But this study provided few discussions on the physical mechanisms that are associated with the improved accuracy. In another previous study [15], several tonal noise sources including the gap turbulence were found, and obvious tones were observed in the acoustic spectra. Nonetheless, the correlations between the noise sources and the tones were not clarified. In a recent study [21], the present authors found that for a voluteless centrifugal fan, the tonal frequencies associated with the *BPF*, are related to surface pressure fluctuations at the blade leading edge (BLE). The high surface pressure fluctuations are caused when turbulence stemming from the gap flow interacts with the BLE close to the shroud.

As the literature review above shows, the aerodynamics of a voluteless fan is influenced by the gap geometry, since turbulent flow develops from the gap and impinges on the blades. It has also been shown that the gap turbulence is one of the predominant tonal noise sources. However, to date, it has not been quantified to which extent the gap geometry influences the tonal noise generation. It is unknown whether noise increments are sensitive to gap geometric changes. As clarified by Guedel [22], turbulent velocity at the fan inlet leads to random blade load fluctuations and broadband noise emission. But, it is not clear whether the changed gap turbulence accounts for only the broadband noise generation or both broadband and tonal noise generation. These concerns motivate the present study.

This study aims to investigate how the tonal noise at the *BPF* is affected when the gap is modified. Three different gap designs are compared with a reference fan (Case 1), which is the same fan in the previous study [21]. Also, the fan performance will be compared and discussed. The location and area of the noise sources responsible for the tonal noise at the *BPF* is addressed.

The numerical simulations in the current study are carried out using a hybrid method of the improved delayed detached eddy simulation (IDDES) [23] and the Ffowcs Williams and Hawkings (FW-H) equation [7], which will be elaborated on in Section 3. The IDDES is used in the flow simulation and the FW-H for the noise prediction. In some previous studies [24,25], the unsteady Reynolds-averaged Navier-Stokes (URANS) equations were adopted for the flow simulation. It was found in a recent study [15] that the aerodynamic forces obtained using the URANS are in good agreement with experimental data. This method coupled with the acoustic analogy well predicts principal tonal noise but not the broadband noise. The reason is that the URANS cannot resolve transient small-scale flow fluctuations that are also noise sources, although large-scale unsteady contents are captured. The IDDES, by contrast, simulates most of the fluctuations despite the modeling of sub-grid scale quantities. Hence, coupling the IDDES with the FW-H equation enables accurate prediction for both tonal and broadband noise, as demonstrated in previous studies on vehicle cooling fans [26,27]. Although the free-field assumption for ducted fans is violated [28], it is still valid for comparison studies. Reese and Carolus [29] showed that for a ducted axial fan, the assumption is still acceptable for frequencies below 1000 Hz. With the blade radial length of 0.0825 m, the sound wavelengths above 1000 Hz are more than 4 times this characteristic length. It is therefore estimated that the sound reflections from the solid surfaces are small for the low frequencies of interest.

2. Application cases

The baseline fan (Case 1) and the three different designs (Case 2, Case 3, and Case 4) are illustrated in Fig. 1. Case 1 is the same fan as the one examined in [21]. As displayed in Fig. 1a, the fan and inlet duct is placed in a downstream duct, and the inlet duct is connected to an upstream duct. This simple geometry layout is designed for the numerical simulations. This simplification reduces the geometry complexity but retains the principal flow and acoustic characteristics.

The fan backplate and blades are the same for all cases and there are seven blades. A clearance (i.e., the gap) is located between the

stationary and rotating parts. For Cases 1, 2, and 3 the shroud geometry is the same, and the flow path of the gap is straight in the streamwise direction. Case 2 has larger gap width (denoted by w), and Case 3 has smaller one than Case 1. The gap width is varied by changing the wall thickness of the inlet duct. In comparisom to the other cases, a curved flow path of the gap is designed for Case 4, while its gap width is the same as Case 1. The fan parameters are listed in Table 1 and the gap width in Table 2. The changes in the gap width and shape are designed to keep the aerodynamic efficiency of the fan nearly the same, since the focus of the present study is to understand whether the small changes affect noise generation. Nevertheless, it will be interesting in the future to study the relationships between operating points, efficiency and noise levels.

The fan rotation speed is 2800 rpm. Given that the fan has seven blades, the *BPF* is 326.7 Hz. The operation point is the same as the off-design point in [21]. This point was selected since the tonal noise at the *BPF* has its highest amplitude here. The mass flow rate was set to 0.467 kgs^{-1} which gave a pressure of 269.6 Pa for Case 1.

3. Numerical methodology

3.1. Computational fluid dynamics

The transport equations of continuity, momentum, and energy equations in the conservation form are generally written as

$$
\frac{\partial \rho}{\partial t} + \nabla \cdot (\rho u) = 0,
$$
$$
\frac{\partial (\rho u)}{\partial t} + \nabla \cdot (\rho u \cdot u) = -\nabla p + \nabla \cdot \tau,
$$
$$
\frac{\partial}{\partial t}(\rho E) + \nabla \cdot (\rho E u) = \nabla \cdot (k \nabla T) - \nabla \cdot (\rho \cdot u) + \nabla \cdot (u \cdot \tau)
$$
(1)

where the total energy $E = e + u \cdot u/2$, e is the internal energy, and k is the thermal conductivity.

If the compressibility is taken into account, the stress tensor τ is defined as

$$
\tau = \mu \left[\nabla u + (\nabla u)^T \right] - \frac{2}{3} \mu (\nabla \cdot u) I
$$
(2)

where μ is the dynamic viscosity. The first term $\mu[\nabla u + (\nabla u)^T]$ is symmetric and anisotropic, which is driven by velocity gradients within the flow [30]. Thus, it accounts for turbulence anisotropy. The second term is isotropic and associated with fluid volume changes due to the compressibility.

The air is considered as an ideal gas. The flow is compressible. A finite volume method is utilized to discretize the continuity, momentum, and energy equations. The method employs a segregated flow solver accomplished with the Semi-Implicit Method for Pressure-Linked Equations (SIMPLE) algorithm [31].

The convection flux on a cell face is discretized utilizing a hybrid second-order upwind and bounded scheme. The diffusion fluxes on both internal and boundary cell faces are discretized with a second-order scheme. The second-order hybrid Gauss-LSQ method is used in gradient computation. A second-order implicit method is taken to discretize the time derivative. The time marching procedure adopts inner iterations at every preconditioned pseudo-time step. All simulations are performed using the commercial software STAR-CCM+ [32]. This setup was validated in the previous study [33], where turbulence-induced acoustic waves transmitting through a cabin window were simulated.

The turbulence is simulated using the IDDES [34] that is combined with the k-ω SST turbulence model. This setup has been tested in several studies on rotating machinery [26,27]. Hereafter, the filtered variables are presented. The IDDES modifies the dissipation in the transport equation of the turbulence kinetic energy k by introducing a hybrid length scale

$$
\widetilde{l}_{DDES} = \widetilde{f}_d (1 + f_e) l_{RANS} + (1 - \widetilde{f}_d) l_{LES}
$$
(3)

where l_{RANS} and l_{LES} are the Reynolds-averaged Navier-Stokes equations (RANS) and LES length scales, respectively. Furthermore, wall modeling in large eddy simulation is taken into account for $\widetilde{f}_d$ and $\widetilde{f}_e$ with the blending functions,

$$
\widetilde{f}_d = \max \left\{ \tanh (C_{dt} r_{dt})^3, \min \left[2 \exp (-9 \alpha^2), 1 \right] \right\},
$$
$$
\alpha = 0.25 - d_w / h_{max}
$$
(4)

where d_w denotes the distance to the wall, and h_{max} is the maximum local grid spacing. The parameter r_{dt} is defined as

$$
r_{dt} = \mu_\tau \left/ \left(\rho \sqrt{\nabla u : \nabla u^T} \kappa^2 d_w^2 \right) \right.
$$
(5)

where μ_τ is the turbulent eddy viscosity, and the von Karman constant $\kappa = 0.41$. The formulation of f_e reads

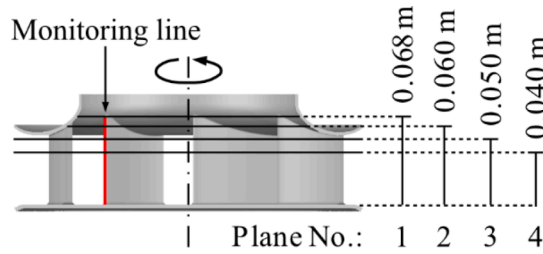$$
f_e = max[(f_{e1} - 1), 0] \psi f_{e2}
$$
(6)

Fig. 2. The cut planes for observing the flow variables in the subsequent analysis. The red line is the monitoring line at the BLE.

where ψ is a low-Reynolds correction that rectifies the activated low-Reynolds number terms of the background RANS model in the LES mode [35] The parameters in Eq. (6) reads

$$f_{e1} = \begin{cases} 2\exp\left(-11.09\alpha^2\right), & \text{for } \alpha \geq 0 \\ 2\exp\left(-9\alpha^2\right), & \text{for } \alpha < 0, \end{cases}$$

$$f_{e2} = 1 - \max\left[\tanh\left(C_t^2 r_{dt}\right)^3, \; \tanh\left(C_l^2 r_{dl}\right)^{10}\right],$$

$$r_{dl} = \mu / \left(\rho \sqrt{\nabla u : \nabla u^T} \kappa^2 d_w^2\right) \tag{7}$$

The coefficients of the IDDES model adopts the default values in the software STAR-CCM+,i. e. $C_{DES,k-\omega} = 0.78$, $C_{DES,k-\varepsilon} = 0.61$, $C_{dt} = 20$, $C_l = 5$, and $C_t = 1.87$ [32]. The notation of the coefficients is the same as in the software user guide [32]. The wall-normal sizes of the first layer cells near all walls fulfill $\Delta y^+ < 1$.

3.2. FW-H equation

A hybrid approach is adopted to predict the noise generated from the flow. In this approach, the IDDES is coupled with Formulation 1A of Farassat [36]. The ambient air density is set to $\rho_0 = 1.225 \text{ kgm}^{-3}$, and the speed of sound $c_0 = 340 \text{ ms}^{-1}$. The Formuation 1A reads

$$p'(x,t) = \frac{1}{4\pi}\int_{f=0}\left\{\frac{1}{1-M_r}\frac{\partial}{\partial\tau}\left[\frac{\rho_0 v_n}{r(1-M_r)} + \frac{p\cos\theta}{c_0 r(1-M_r)}\right]\right\}_{\tau_e} dS \; + \frac{1}{4\pi}\int_{f=0}\left[\frac{p\cos\theta}{r^2(1-M_r)}\right]_{\tau_e} dS \tag{8}$$

where $r = |x - y|$, and $M_r = (x - y) \cdot v/(rc_0)$. The variable v_n is the local surface normal velocity, and τ_e denotes the emission time. Besides, $\cos\theta = (x - y) \cdot n$, where n is the unit vector normal to the surface.

According to Neise [37], the fan noise generation at low Mach numbers is dominated by dipole noise sources that are derived based on the FW-H equation. The same observation has also been reported for the current voluteless centrifugal fan using URANS coupled with Formulation 1A [15,24]. Hence, the noise prediction in this study considers only an impermeable integral surface for Formulation 1A. The integral surface consists of the fan blades, shroud, and backplate (see Fig. 1a), this approach is chosen so that the sources for the *BPF* can be compared. This method agreed well in [38] where the unsteady flow in a centrifugal fan was studied and evaluated with experiments. The upstream and downstream ducts, as well as the fan inlet duct, are neglected. This treatment disregards the acoustic reflection from the duct walls to resemble the conditions in the experimental rig.

3.3. Numerical settings

The entire computational domain is divided into stationary and rotating parts. The parts contained within the ducts are stationary, whereas the part inside the fan is rotating. The meshes of the stationary and rotating meshes are not conformable at the interfaces between them.

The under-relaxation factors for the velocity and pressure in the segregated flow solver are set to 0.7 and 0.4, respectively. The under-relaxation factor for the turbulence equations is 0.7.

The mass-flow boundary condition is set at the inlet, with a uniform velocity distribution. The modeled turbulence intensity is set to $I = 4\%$ according to $I = 0.16(R_e)^{-1/8}$ [32]. Here R_e is computed based on the inlet diameter and the streamwise velocity at the inlet. The modeled turbulence length scale is set to $\ell = 0.5$m based on $\ell = 0.7d_3$ where d_3 is the upstream duct diameter. The turbulence intensity calculation at the inlet according to [32], was validated in [39] for a centrifugal fan with an inlet duct. The result was in good agreement with the experimental data. The pressure-outlet boundary condition is set at the outlet with the static pressure of 101325 Pa, which is the reference pressure (p_{ref}) in the ambient air. The no-slip boundary condition is specified on all walls.

The time step is set to $\Delta t = 2.0 \times 10^{-5}$ s, leading to a maximum convective Courant number of around 10. This value fulfills the numerical stability required for the implicit time-marching method. The maximum number of inner iterations per time step is set to 12.

The sampling period of the noise is 0.3 s for all cases, corresponding to 14 fan revolutions. The same period was considered in [21],
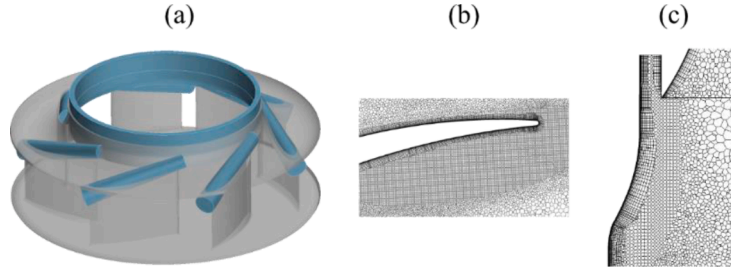
Fig. 3. a) Mesh refinement regions (blue) at the inlet gap and blades top region. Mesh cells near b) the blade trailing edge and c) the inlet gap.

Table 3
The mesh parameters.

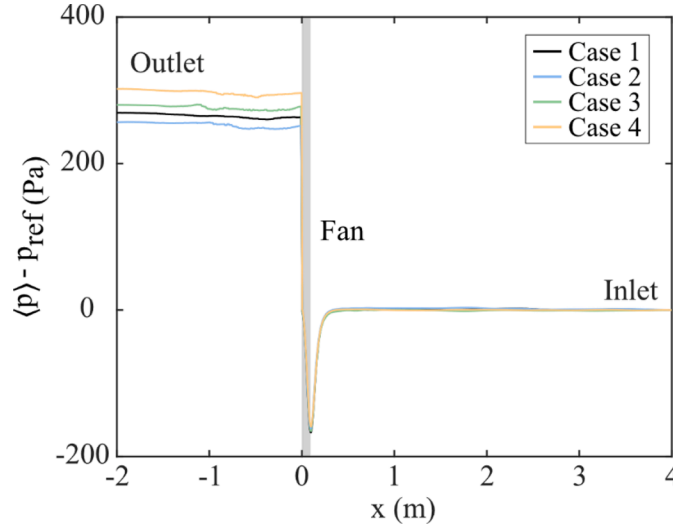|	Case 1	Case 2	Case 3	Case 4
Total number of cells	52×10^6	52.2×10^6	52×10^6	53.2×10^6
Number of cells in the rotating zone	41.9×10^6	42.1×10^6	41.9×10^6	43.1×10^6
Maximum height of first-layer cells near blade walls Δy^+	0.73	0.73	0.73	0.73
Cell growth ratio	1.05	1.05	1.05	1.05

Fig. 4. The pressure along the axial axis of the fan across the computational domain. $\mathrm{x} = -2$ corresponds to the location near the outlet and $\mathrm{x} = 4$ near the inlet. The fan location is marked out with the gray zone.

and the results agreed well with the experimental results. The sampling time interval is $5\Delta t$. The PSD is calculated using the von Hann window for 3000 samples per signal section, which leads to a frequency resolution of around 3 Hz, and no overlapping between the signal sections.

Four cut planes (Planes 1-4) across the fan are specified to observe the flow quantities in the subsequent analysis. The cut planes are shown in Fig. 2. The red line is a monitoring line positioned at the BLE which extends from the backplate to the shroud.

4. Computational meshes

We adopt the same mesh generation strategy that was developed and validated in [21], where the fan is the same as Case 1. A polyhedral mesh generation method was used to produce prism layers near the walls and polyhedral cells in the rest of the computational domain. The use of polyhedral cells for turbomachines has been shown in [24,40] to be a good choice. The growth rate is set to 1.05, as suggested in [41]. The most important findings in the mesh study performed in [21] were that a local refinement has to be made at the regions extending from the gap to the BLE and along the blade to the blade trailing edge. These mesh refinement regions (blue) are illustrated in Fig. 3. The mesh parameters are listed in Table 3. The refined mesh resolution enables the LES mode for the IDDES, which is controlled by $\widetilde{f}_d$ in Eq. (4). $\widetilde{f}_d$ blends between the URNAS and LES mode, which depends on the grid spacing and the
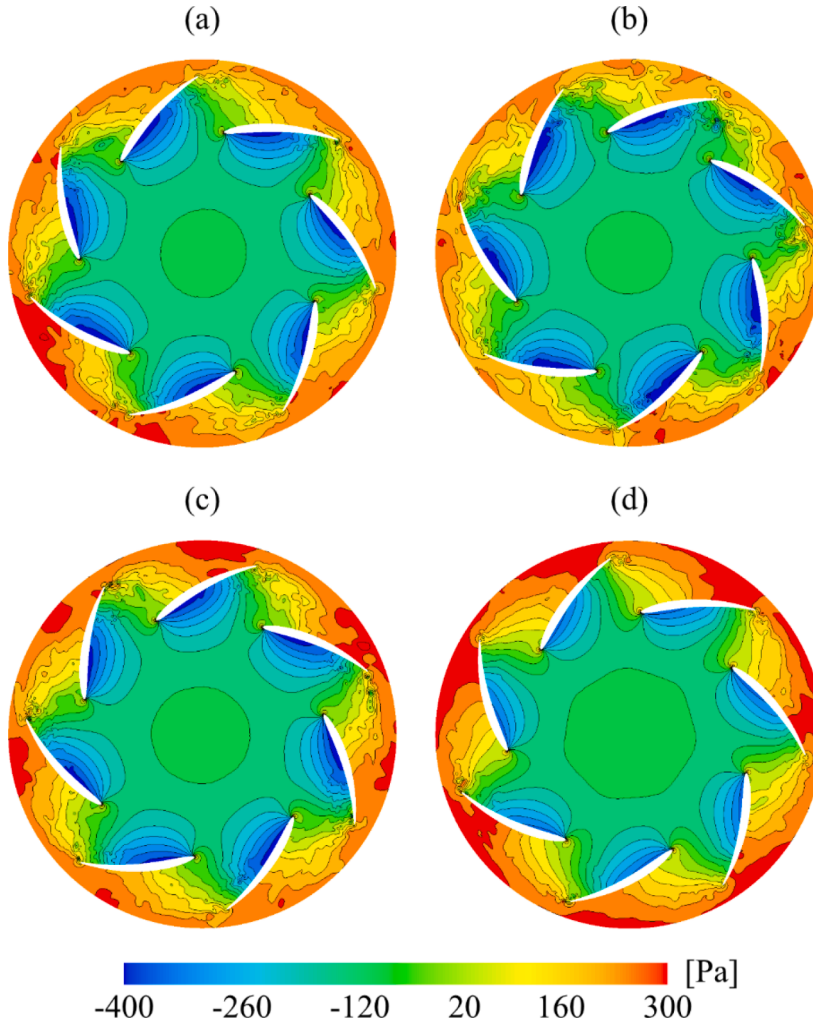
Fig. 5. The instantaneous pressure in Plane 3: (a) Case 1, (b) Case 2, (c) Case 3, and (d) Case 4.

wall distance.

The mesh size in the upstream duct and downstream duct is 55 cells per meter. According to [30] it should be at least 20 cells per wavelength for the shortest wavelength. This corresponds to a minimum frequency of 124 Hz for this mesh, which is well below the tonal noise at the $BPF = 326.7$ Hz.

5. Results and discussion

5.1. Fan performance

The static pressure excluding the reference pressure ($p_{ref} = 101325$ Pa) is displayed along the axial symmetric line for all cases in Fig. 4. All cases show consistent pressure amplitudes in the upstream duct of the fan, while differences are seen downstream. The difference in pressure rise downstream of the fan is only due to the gap design. Compared to Case 1, the gap width is larger in Case 2 and smaller in Case 3. Among these three cases, the pressure rise is smallest in Case 2 and largest in Case 3. Therefore, increasing the gap width worsens the fan performance. The same finding was also clarified in a previous study [12]. However, the anomaly is found in Case 4. This case produces larger pressure rise than Cases 1-3, even though its gap width is the same as Case 1. The geometric differences between Cases 1 and 4 are that the gap of Case 4 has a longer streamwise length and a curved shape. These geometric changes lead to an increase in the pressure rise.

Fig. 5 shows the instantaneous pressure in Plane 3 (see the plane position in Fig. 2). The pressure increase in the channel between two neighboring blades is largest in Case 4. This also demonstrates the phenomenon observed in Fig. 4 that the pressure at the fan outlet is highest in Case 4. Unlike from Case 4, there are significant pressure fluctuations near the blade trailing edge in Cases 1-3. It is known that the fluctuating pressure distribution is caused by turbulent structures in the flow and affects the fan performance.
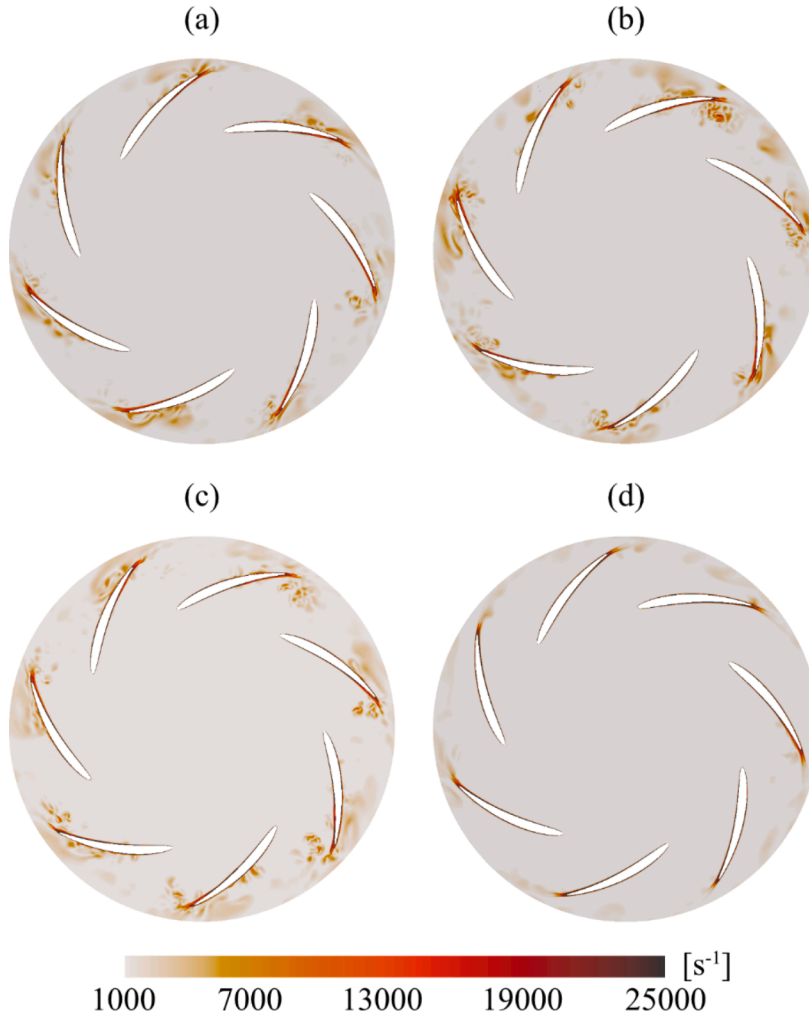
Fig. 6. The instantaneous vorticity magnitudes near the shroud, which are visualized in Plane 4: (a) Case 1, (b) Case 2, (c) Case 3, and (d) Case 4.

The contours of the vorticity magnitudes are illustrated for all cases in Plane 4 in Fig. 6. For Cases 1-3, there are regions of large vorticity on the pressure and suction sides of the blades, near the blade trailing edges. The locations agree with the nonuniform pressure in Fig. 5. The large vorticity regions are caused by flow separation according to previous studies [15,17]. As clarified by Lee [14], the gap flow produces the trailing edge separation, which affects the fan performance. Case 4 has fewer vortices in these regions.

The instantaneous surface pressure magnitudes over the whole blade surface at the intersection of Plane 4 are displayed in Fig. 7. Here, η_{chord} is the nondimensional blade chord length measured from the leading edge ($\eta_{chord} = 0$) to the trailing edge ($\eta_{chord} = 100$). The reference pressure, p_{ref}, is excluded from the static pressure shown in the figure. The pressure on the pressure side near the blade trailing edges shows different distributions among the blades for Cases 1-3, whereas it is more stable in Case 4. Cases 1 and 4 have the same gap width, but Case 4 has a significantly longer gap length than Case 1. Therefore, the longer gap length stabilizes the flow, as shown in Figs. 6 and 7.

5.2. Interaction between inlet-gap turbulence and blades

The root mean square (RMS) pressures at the monitoring line at the BLE (described in Fig. 2) are illustrated for all cases in Fig. 8a. The line follows the blade rotation and the surface pressure is monitored during 12 fan revolutions. At the position nearest the shroud (Plane 1), the highest RMS pressure is observed for all cases. The RMS pressures have the same physical behavior for all four cases and when the distance to the shroud increases, the RMS pressure decays. From Plane 1 to the backplate, Case 2 has the lowest RMS pressure, and Case 4 the highest. At the backplate, al cases have the same RMS pressure.

The time-averaged of the surface pressures at the BLE are shown at different positions for all cases in Fig. 8b. The maximum values for all cases occur at Plane 1 (shroud), whereas at the backplate the values are negative. The amplitudes of the maximum and minimum pressure (error bar) are largest at Plane 1 and they decay when the distance from the shroud increases, for all cases. At Plane 1, Case 4
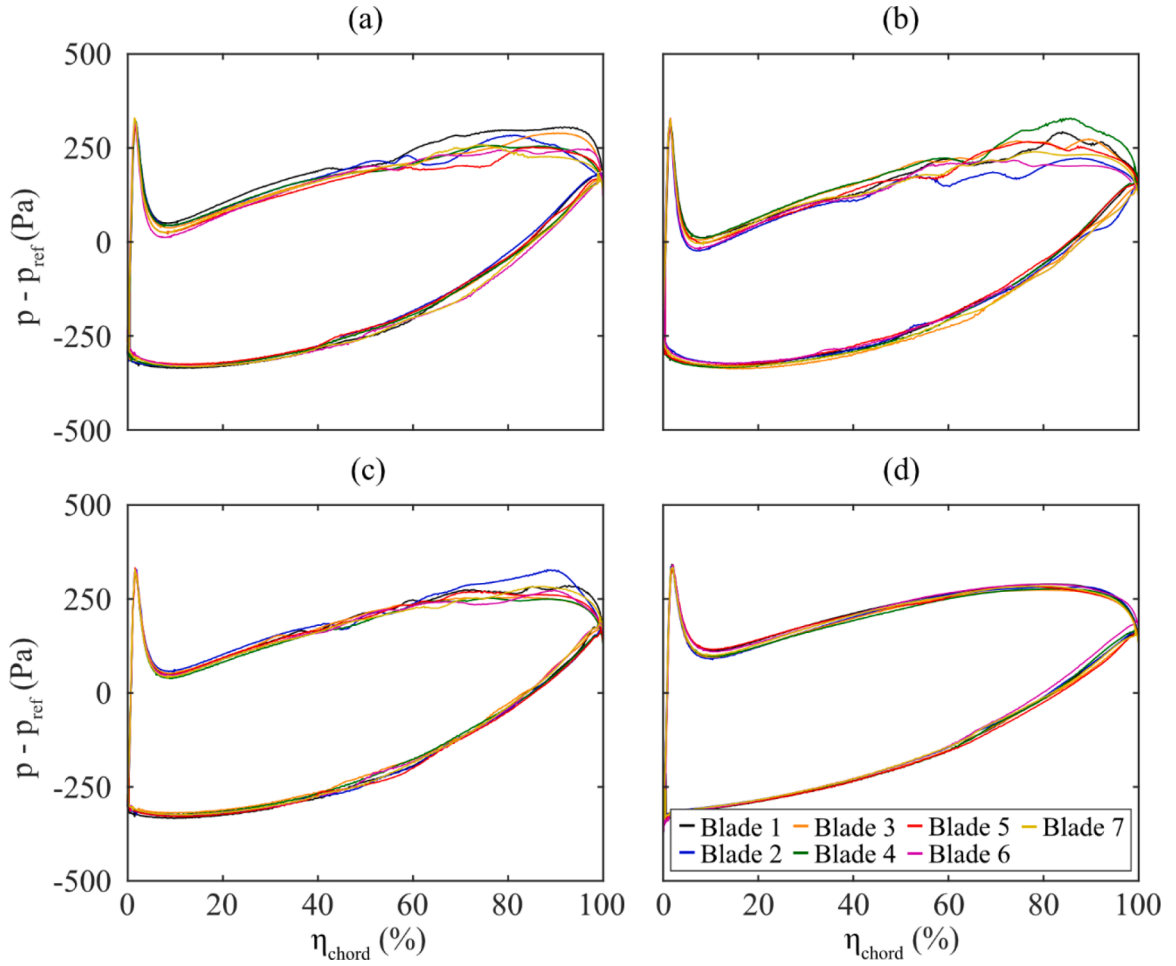
Fig. 7. The instantaneous surface pressure on the blades in the sectional plane, Plane 4: (a) Case 1, (b) Case 2, (c) Case 3, and (d) Case 4.
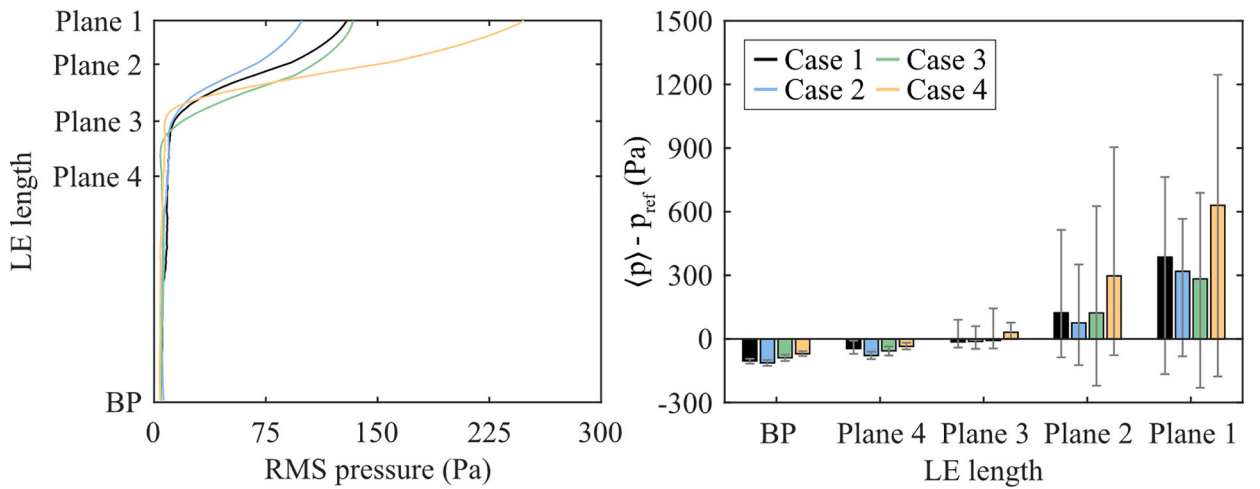
Fig. 8. (a) The RMS values of the pressure fluctuations for 12 fan revolutions, on one blade at the monitoring line, i.e. BLE; (b) the time-average pressure and error bars showing the minimum and maximum pressure. Here, BP corresponds to the backplate.
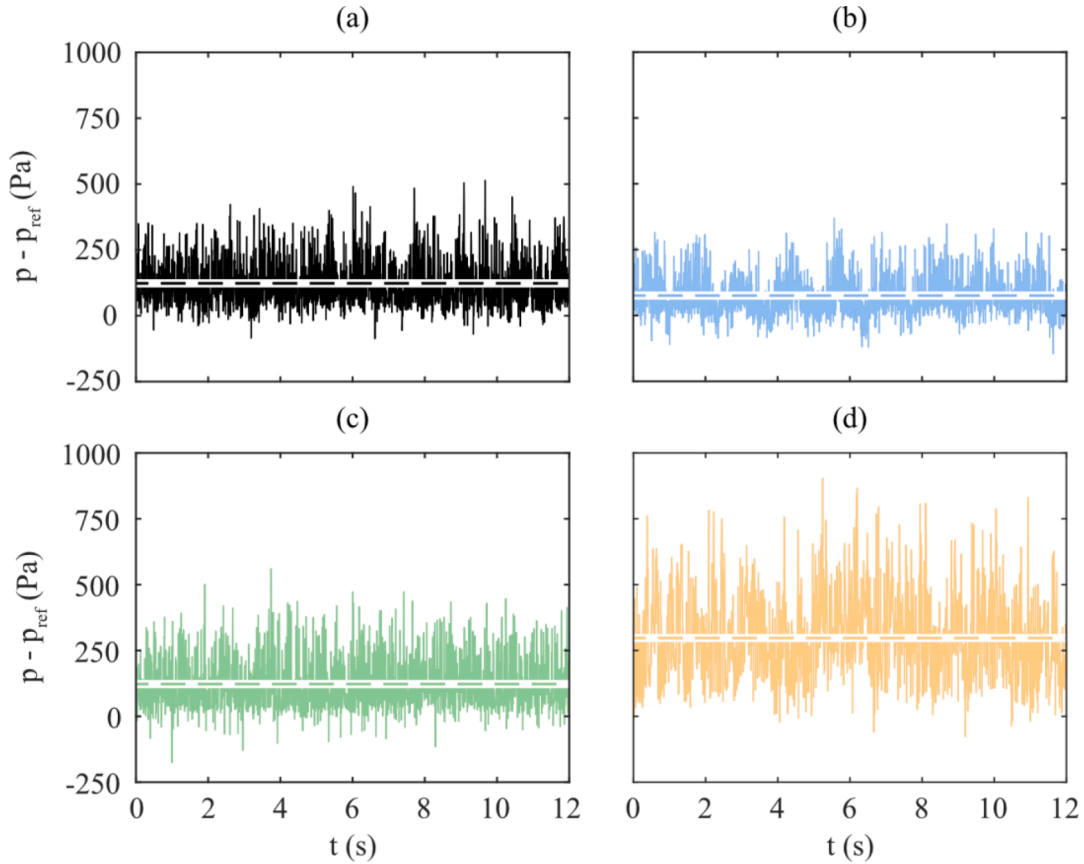
Fig. 9. The time history of surface pressures along the BLE at point 2 (a) Case 1, (b) Case 2, (c) Case 3, and (d) Case 4. Dashed lines show the time-averaged pressure values.

has the highest amplitude. Case 2 has the lowest amplitudes at all positions. At Plane 2 and 3, the maximum positive fluctuations are larger than the magnitude of the negative ones, and it is the same for all cases. It is clear that Case 2 has the smallest pressure fluctuations at the BLE.

Fig. 9 shows the time history of the surface pressure for all cases at the point in the BLE monitoring line intersected by Plane 2. The time history is shown over 12 fan periods. The dashed lines indicate the average values for the cases. For Cases 1, 3, and 4, pressure fluctuations with large amplitudes and high frequencies are observed. Fluctuations are also obvious for Case 2, but the amplitudes are smaller than for the other cases. This observation supports the finding in Fig. 8b, which shows that Case 2 has the narrowest fluctuating range in terms of the maximum and minimum amplitudes. Moreover, a periodic low-frequency fluctuation in relation to the fan rotation is seen for Case 2, which was also found in [15,21], but there is no clear periodic low-frequency fluctuation in the other cases. A common behavior of all cases is that the maximum positive fluctuations are larger than the magnitudes of the negative ones. The reason is that the gap vortices impinge the BLE cause large positive pressure fluctuations which happens rarely, this is called skewness and the surface pressure on the BLE is skewed towards the positive side.

The contours of vorticity magnitudes $\| \vec{\omega} \|$ in Plane 1 are shown for all cases in Fig. 10. The position of Plane 1 is located near the fan inlet, as illustrated in Fig. 2. Regions with large vorticity magnitudes are detected for Cases 1, 3, and 4. These regions move along the shroud and interact with the BLE. According to [21], surface pressure fluctuations are caused when turbulent vortices, stemming from the fan inlet gap, interact with the BLE close to the shroud. However, Case 2 has no regions with high vorticity magnitudes, which is in agreement with small RMS pressure in Figs. 8a and 9b.

The contours of the velocity magnitudes in a y-z plane are defined as $|v_R| = \sqrt{v_y^2 + v_z^2}$ (coordinate axes defined in Fig. 1), and the streamlines of the relative velocity vectors in Plane 1 are displayed for all cases in Fig. 11. Note that the axial velocity component along the fan rotation axis is excluded from the vectors. For Cases 1, 3, and 4, there are regions with large velocity magnitudes near the shroud (Plane 1). These regions appear periodically in relation to the blade positions. These regions cannot be observed for Case 2. This suggests that the flow near the shroud is highly fluctuating due to the gap turbulence for Cases 1, 3, and 4 and that Case 2 has less turbulence above the blades (near the fan inlet). The phenomenon of large v_R magnitudes was also found in previous studies [18,21].

The iso-surfaces of the vorticity magnitude of $\| \vec{\omega} \| = 2 \times 10^4$ s^{-1}, colored by the instantaneous pressure, near the gap are shown in Fig. 12. There are more iso-surfaces in Cases 1, 3, and 4, and intensive turbulent structures are found to interact with the BLE in
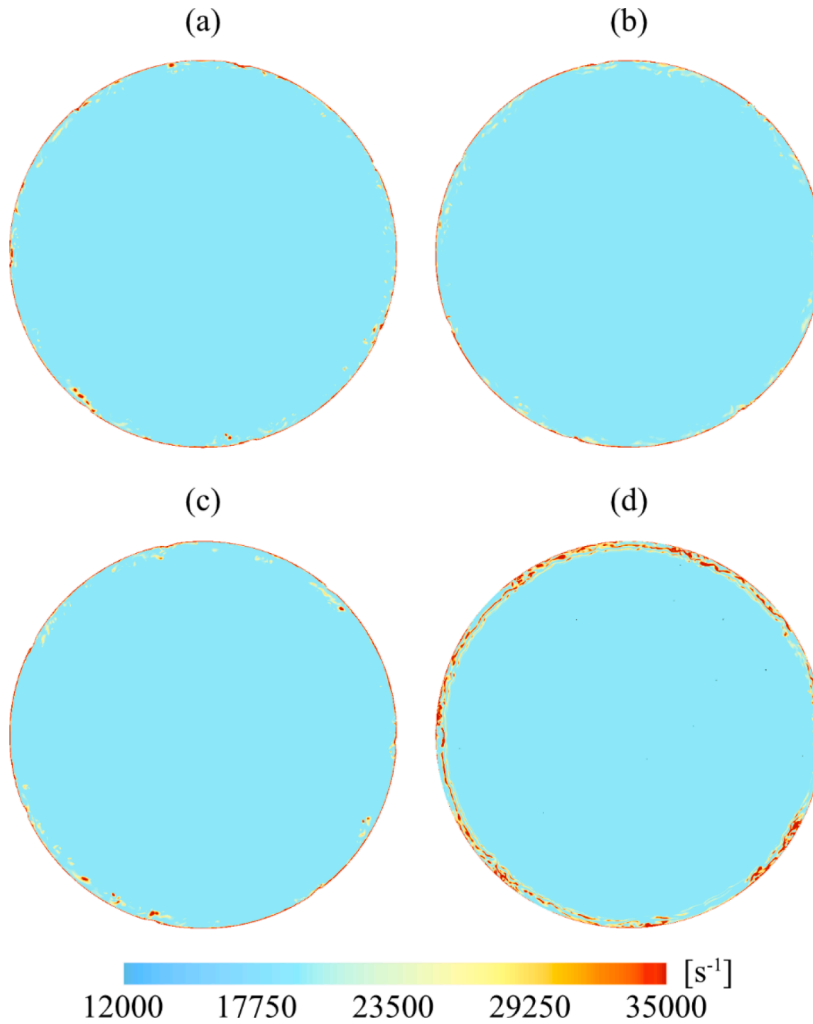
Fig. 10. Instantaneous vorticity magnitudes near the shroud are visualized in Plane 1: a) Case 1, b) Case 2, c) Case 3, and d) Case 4.

relatively larger BLE regions, as compared to Case 2. The gap flow develops along the shroud surface and only interacts with the top side of the BLE, that is, the connection position of the BLE and shroud. In Case 2, the gap flow is less turbulent. Additionally, the instantaneous pressure in Case 2 is qualitatively smaller than in the other cases.

As illustrated in Fig. 12, the flow involves two physical mechanisms: the evolution of turbulent vortices, and the interaction of the blade with stretched vortices. According to Howe's theory of aerodynamic sound [42], the local fluctuations induced by the vortices are responsible for the generation of broadband noise, since the length and time scales of the turbulence have a broadband characteristic spanning a wide range of wavenumbers and frequencies. Fig. 13 shows the power spectral density (PSD) of the pressure fluctuations ahead of the BLE. The broadband characteristic is observed in all cases and is case dependent. Meanwhile, Howe's theory highlights that the fluid-structure interactions mainly contribute to the generation of tonal noise. It is worth noting that some broadband noise can also be generated from the interactions due to the local turbulence, but it is much smaller than the tonal noise.

5.3. Turbulence-induced tonal noise

In the previous studies of Case 1 [15,23], it was shown that the PSD of the noise at the tonal frequency, *BPF*, was in closer agreement upstream of the fan (M1) than downstream (M2), see Fig. 1. The SPL of the noise at the microphone M1 is compared in Fig. 14. The highest *BPF* amplitude is observed for Case 4, which is 4 dB higher than Case 1. Comparing Cases 1-3 where only the gap width is changed, Case 2 with the largest gap width has the lowest *BPF* magnitude, and Case 1 with the medium gap width has the medium *BPF* magnitude. This indicates that increasing the gap width leads to a reduction in the tonal noise generation. Moreover, a similar trend is observed for the broadband noise, i.e., magnitudes increase sequentially in Case 2, Case 3, and Case 1. This trend is consistent with the observation in Fig. 13, where the broadband content in the PSDs of the pressure fluctuations decrease with increasing the gap width. In contrast to Cases 1-3, Case 4 produces larger tonal noise at the *BPF*. The reason for this might be that the longer spacing in the gap in
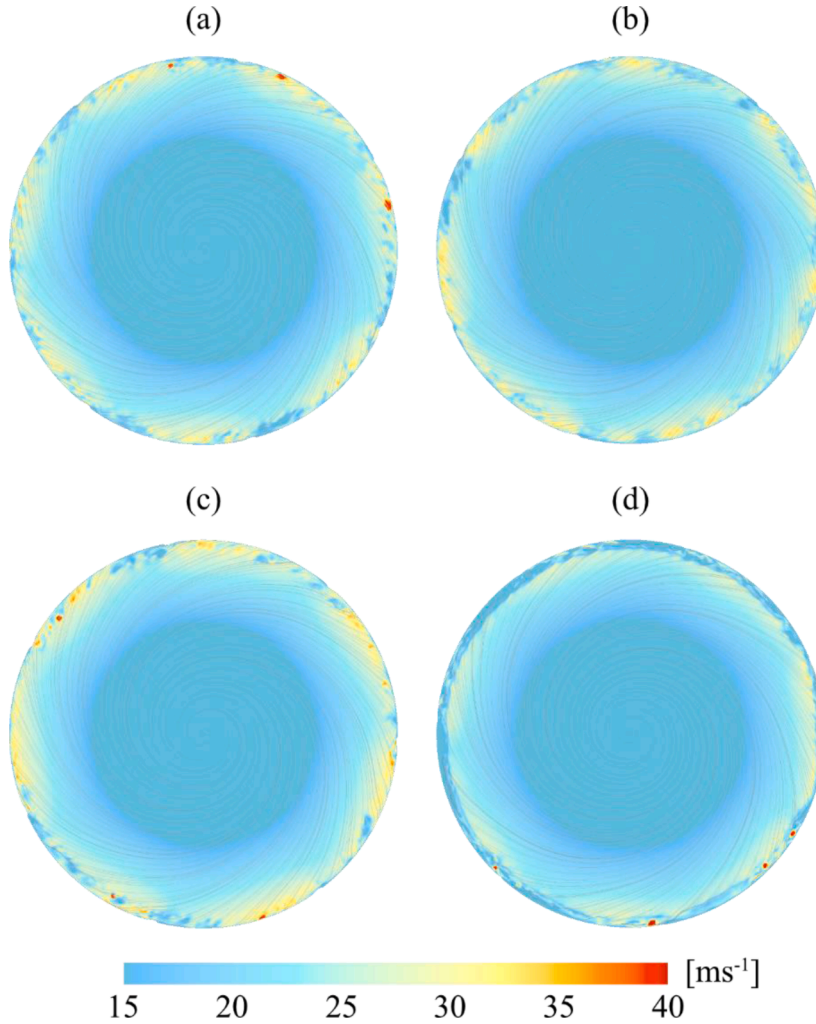
Fig. 11. Instantaneous velocity magnitudes $|v_R| = \sqrt{v_y^2 + v_z^2}$ visualized in Plane 1: a) Case 1, b) Case 2, c) Case 3, and d) Case 4.

Case 4 triggers more stretched vortices compared with Case 1. These results agree with the results from Figs. 8–11, where Case 2 had the lowest surface pressure fluctuations on the BLE.

As displayed in Fig. 14, the tonal noise at the BPF in the reference configuration Case 1 is 67.5 dB. With respect to this reference, different tonal noise levels are found for the other cases. Accordingly, the noise impact on the IEQ is mitigated by 5.7 dB at 326.7 Hz in Case 2, but deteriorates by 0.5 dB in Case 3 and by 4 dB in Case 4.

5.4. Spectral analysis of tonal noise sources

Based on the band-filtered PSD of surface pressure fluctuations, the location and magnitudes of dominant tonal noise sources are evaluated. The results at the tonal frequency of $BPF = 326.7$ Hz are illustrated in Fig. 15. The location of the highest surface pressure fluctuations is at the same position (the top side of the BLE that is connected to the shroud) for all cases. Besides, this position is found with high vorticity magnitudes, high RMS pressure, and the largest pressure fluctuation. The differences between the Cases are the maximum magnitude and the size of the high-magnitude region. Case 4 has the largest sound pressure (see Fig. 13), and it has also the largest area and magnitude at the tonal frequency. The high energy locations are consistent with the surface pressure fluctuations indicated in Fig. 8. The high energy is caused by the interaction between the gap turbulence and the BLE [21].

Additionally, in Cases 1, 2, and 3, small magnitudes are seen at the blade trailing edge close to the shroud. In contrast, Case 4 does not show such a region. This agrees with the findings in Figs. 5–7, where high vorticity magnitudes and surface pressure fluctuations were found at the same location for Cases 1, 2, and 3 but not for Case 4. The large vorticity regions are caused by the flow separation. According to previous studies [15,17], the flow separation is triggered by the turbulence from the gap. Therefore, the gap turbulence is the cause of these tonal noise regions. But it should be recalled that the magnitude of the surface fluctuations is much smaller in the separation region than at the BLE.
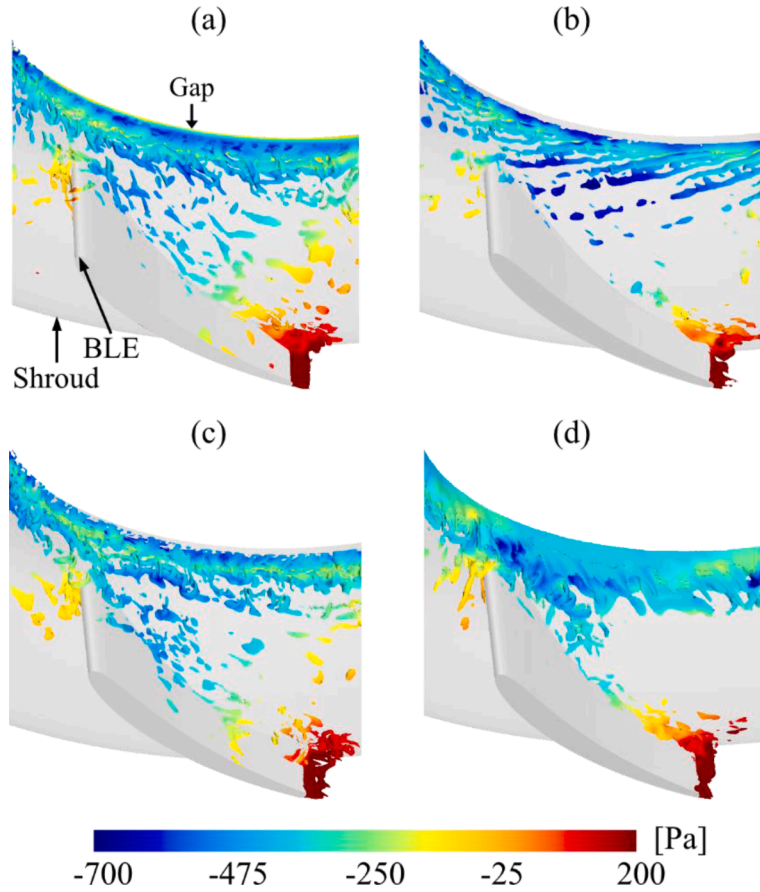
Fig. 12. Iso-surfaces of the vorticity magnitudes at $\| \vec{\omega} \| = 2 \times 10^4$ s^{-1}, colored by the instantaneous pressure: a) Case 1, b) Case 2, c) Case 3, and d) Case 4.

There is a clear contradiction between the aerodynamic performance and the acoustic emission. As can be seen in Fig. 4, the pressure rise decreases from Case 4, Case 3, Case 1 to Case 2. However, Fig. 14 shows that the noise is reduced in the reverse order: Case 2, Case 1, Case 3 and Case 4. For Case 4 exhibiting the largest pressure rise, vortices are less intensive near the blade training edge in Plane 4 that is well inside the blade passage (see Fig. 6), and at the same position there are less pressure fluctuations (see Fig. 7). Thus, the aerodynamic performance is related to the turbulence inside the blade passage. However, Case 4 is the worst acoustic case. This is attributed to the strongest gap turbulence near the wall at the blade leading edge, as indicated in Plane 1 in Fig. 10. The turbulence from the gap is ingested into the blade passage and results in the strongest pressure fluctuations, which are observed in Fig. 15. The synthesis of these effects suggests the physical mechanisms that given the turbulence at the entry (around Plane 1) becomes stronger, the flow inside the blade passage (around Plane 4) is stabilized. Consequently, the fluctuations near the blade trailing edge are mitigated, resulting in improved aerodynamic performance.

6. Conclusion

Four different voluteless centrifugal fans for HVAC systems are compared for their aerodynamic and aeroacoustic characteristics. The study is motivated by findings in a previous study by the present authors, that the gap flow is responsible for tonal noise. The flow is simulated by a hybrid method coupling the IDDES with Formulation 1A of Farassat.

With respect to Case 1, Cases 2 and 3 differ in the gap width, and Case 4 in the longer streamwise length and curved shape of the gap. The comparison of Cases 1–3 shows that increasing the gap width reduces the pressure rise downstream of the fan. Case 4 produces the largest pressure rise than the other cases.

Regions with high vorticity magnitudes are found in the channel between two neighboring blades near the blade trailing edges close to the shroud (Plane 4), for Cases 1–3. Moreover, the high vorticity magnitudes cause different surface pressure distributions among the blades, where Case 2 has the largest difference. This results in a uniform pressure rise, in the channel between two neighboring blades. The regions with high vorticity magnitude could not be found for Case 4 and it has the same pressure distribution for all blades.

The four designs show a similar trend of the RMS pressure. The RMS pressure is largest at the shroud and decays when the distance
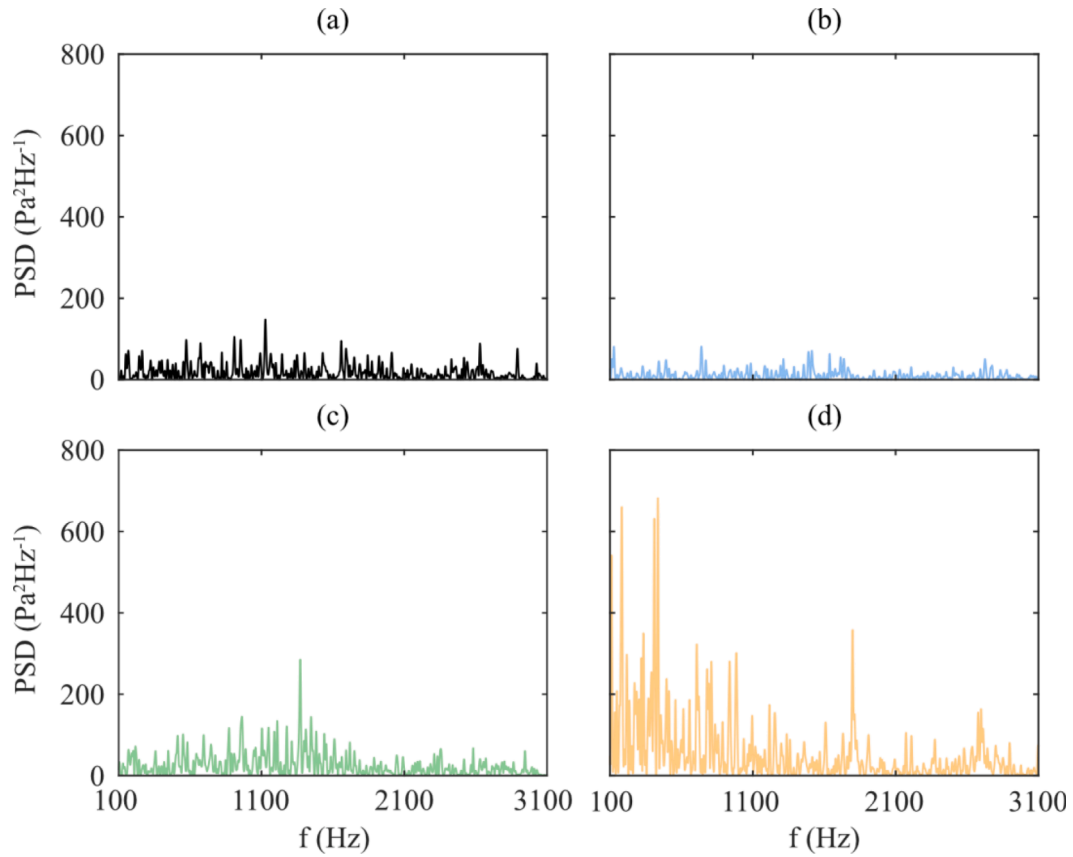
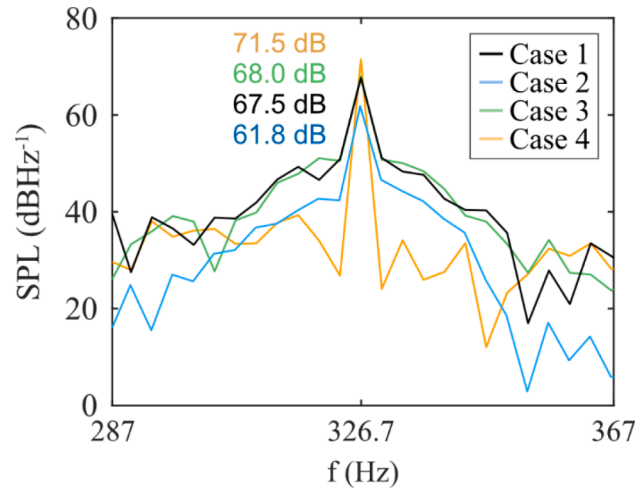**Fig. 13.** PSD of pressure fluctuations at the BLE (a) Case 1, (b) Case 2, (c) Case 3, and (d) Case 4.

Fig. 14. The SPL of the sound pressure at the microphone M1 upstream of the fan. The tonal frequency $BPF = 326.7$ Hz. The SPL values of the tones are presented.

to the gap increases. Moreover, at the position of 20% blade width from the shroud (Plane 3 shown in Fig. 8), the RMS pressure reaches the smallest value. Case 2 has the lowest RMS amplitudes at all positions and Case 4 has the highest.

Spectral analysis is performed for the surface pressure fluctuations and the sound pressure at the microphones M1. There are regions with high energy identical to the locations where the gap turbulence evolves and accounts for the impingement on the BLE, for all cases. Case 2 has the lowest tonal noise at the BPF and Case 4 has the highest. This agrees with the observations of the pressure
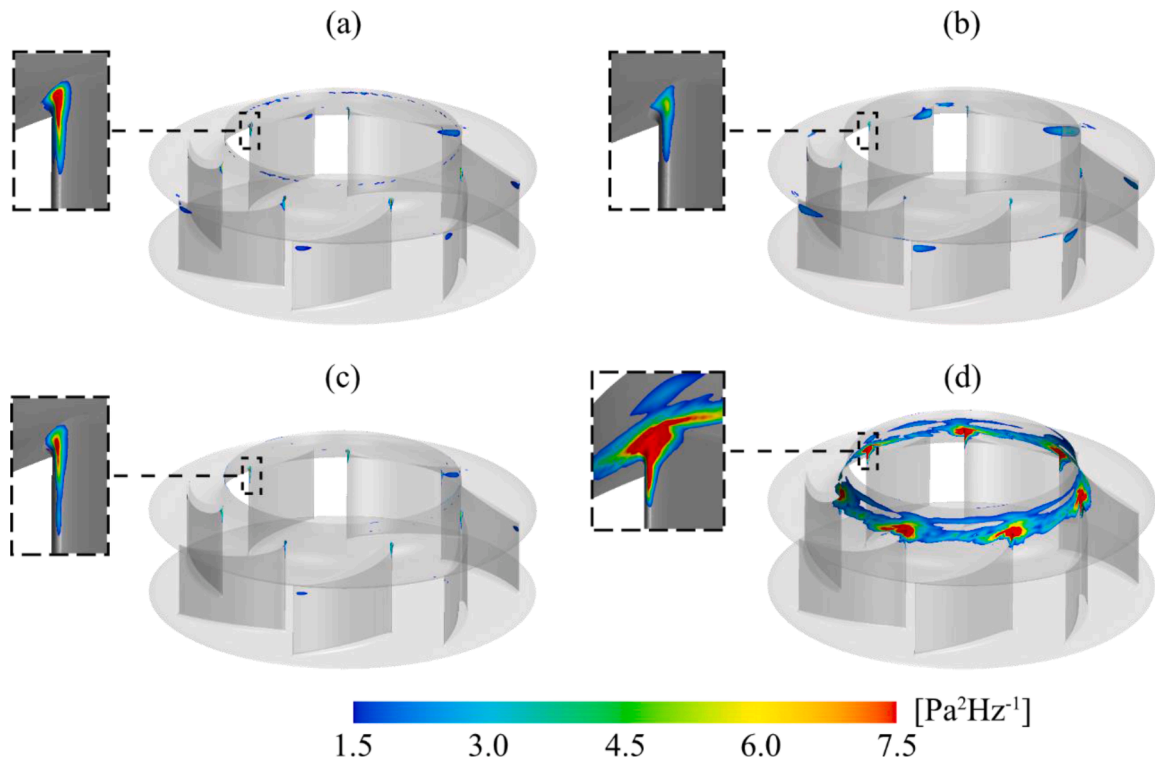
Fig. 15. The PSD of surface pressure fluctuations at $BPF = 326.7$ Hz. (a) Case 1, (b) Case 2, (c) Case 3, and (d) Case 4.

fluctuations. The spectral analysis also indicates that Case 2 has the lowest magnitude at the BLE close to the shroud and that Case 4 has the highest.

Additionally, small magnitudes of pressure fluctuations are seen at the blade trailing edge close to the shroud for Case 1, 2, and 3. In contrast, no fluctuations are seen in these regions for Case 4. This agrees with the observations of the surface pressure distribution at the pressure side of the blade close to the trailing edges. Therefore, the gap turbulence dominates these regions as well.

By redesigning the gap, the aerodynamic and acoustic performances are affected with opposite trends. The comparison of Cases 1–3 shows that increasing the gap width leads to a reduction in the generation of the BPF tonal noise, as well as the broadband noise. However, this change of the gap width worsens the aerodynamic performance in generating the pressure rise. Case 4 has longer gap spacing than Case 1, although both have the same gap width. The long gap design increases the noise generation but improves the pressure rise. The opposite effects on the acoustics and aerodynamics agree with the findings for Cases 1–3. In all configurations, Case 4 has the worst acoustic performance but the best aerodynamic performance. From the analysis of the pressure fluctuations and vortices at the different fan locations, it can be deduced that the fan noise is increased by the turbulence ingested from the gap region, and that the aerodynamics is reduced by the turbulence inside the blade passage near the blade trailing edge. The increased turbulence from the gap interconnects the reduced turbulence near the blade trailing edge. In other words, the stronger turbulence at the entry near the gap can stabilize the flow inside the fan blade passage, leading to less fluctuations and thus to a better aerodynamic performance.

CRediT authorship contribution statement

M. Ottersten: Conceptualization, Methodology, Software, Formal analysis, Investigation, Writing – original draft, Writing – review & editing, Visualization. **H.D. Yao:** Writing – review & editing, Supervision. **L. Davidson:** Writing – review & editing, Supervision.

Declaration of Competing Interest

The authors declare that they have no known competing financial interests or personal relationships that could have appeared to influence the work reported in this paper.

Data Availability

The data that support the findings of this study are available from the corresponding author upon reasonable request.

References

[1] B. Berglund, T. Lindvall, D. Schwela, New guidelines for community noise, Noise Vib. Worldw. 31 (2000) 24–29.

[2] M. Azimi, Noise reduction in buildings using sound absorbing materials, J. Archit. Eng. Technol. 6 (2017).

[3] J. Seabi, K. Cockcroft, P. Goldschagg, M. Greyling, A prospective follow-up study of the effects of chronic aircraft noise exposure on learners' reading and comprehension in South Africa, J. Expo. Sci. Environ. Epidemiol. 25 (2015).

[4] M. Klatte, K. Bergstrom, T. Lachmann, "Does noise affect learning? A short review on noise effets on cognitive performance in children", Front. Psychol. 4 (2013).

[5] L.M. Wang, C.C. Novak, Human performance and perception-based evaluations of indoor noise criteria for rating mechanical system noise with time-varying fluctuations, ASHRAE Trans. 116 (2010) 553–568.

[6] V. Pommier-Budinger, O. Cherrier, Baffle silencer with tunable resonators for adaptive control of variable tonal noise, J. Vib. Control 21 (2015) 1801–1809.

[7] J.E. Ffowcs Williams, D.L. Hawkings, Theory relating to the noise of rotating machinery, J. Sound Vib. 10 (1969) 10–21.

[8] D. Wolfram, T.H. Carolus, Experimental and numerical investigation of the unsteady flow field and tone generation in an isolated centrifugal fan impeller, J. Sound Vib. 329 (2010) 4380–4397.

[9] M. Sanjose, S. Moreau, Direct noise prediction and control of an installed large low-speed radial fan, Eur. J. Mech. B. Fluids 61 (2017) 235–243.

[10] F. Pérot F, M.S. Kim, V.L. Goff, X. Carniel, Y. Goth Y, C. Chassaignon, Numerical optimization of the tonal noise of a backward centrifugal fan using a flow obstruction, Noise Control Eng. J. 61 (2013) 307–319.

[11] J.S. Choi, D.K. McLaughlin, D.E Thompson, Experiments on the unsteady flow field and noise generation in a centrifugal pump impeller, J. Sound Vib. 263 (2003) 493–514.

[12] C. Hariharan, M. Govardhan, Effect of inlet clearance on the aerodynamic performance of a centrifugal blower, Int. J. Turbo Jet Engines 33 (2016) 215–228.

[13] Y. Lee, Impact of fan gap flow on the centrifugal impeller aerodynamics, J. Fluids Eng. 132 (2010) 1–9.

[14] Y. Lee, V. Ahuja, A. Hosangadi, R. Birkbeck, Impeller design of a centrifugal fan with blade optimization, Int. J. Rotating Mach. (2011).

[15] M. Ottersten, H.-D. Yao, L. Davidson, Numerical and experimental study of tonal noise sources at the outlet of an isolated centrifugal fan, ArXiv 2011 (2020) 13645.

[16] M. Ubaldi, P. Zunino, A. Cattanei, Relative flow and turbulence measurements downstream of a backward centrifugal impeller, J. Turbomach. 115 (1992) 543–551.

[17] M.W. Johnson, J. Moore, The development of wake flow in a centrifugal impeller, J. Eng. Power 102 (1980) 382–389.

[18] L. Mongeau, D. Thompson, D. McLaughlin, Sound generation by rotating stall in centrifugal turbomachines, J. Sound Vib. 163 (1993) 1–30.

[19] Y.H. Yu, Rotor blade-vortex interaction noise, Progr. Aerosp. Sci. 36 (2000) 97–115.

[20] R. Schaefer, M. Boehle, Influence of the mesh size on the aerodynamic and aeroacoustics of a centrifugal fan using lattice-Boltzmann Method, in: 23rd International Congress on Acoustics in Aachen, 2019, pp. 1882–1889.

[21] M. Ottersten, H.-D. Yao, Tonal noise of voluteless centrifugal fan generated by turbulence stemming from upstream inlet gap, Phys. Fluids 33 (2021), https://doi.org/10.1063/5.0055242.

[22] A. Guedel, Acoustique des ventilateurs, Edirion PYC (1999). Livres, Paris.

[23] M.L. Shur, P.R. Spalart, M.K. Strelets, A.K. Travin, A Hybrid RANS-LES approach with delayed-DES and wall-modelled LES capabilities, Int. J. Heat Fluid Flow 29 (2008) 1638–1649.

[24] M. Ottersten, H.D. Yao, L. Davidson, Unsteady simulation of tonal noise from isolated centrifugal fan, engrXiv (2020), https://doi.org/10.31224/osf.io/yx7rj.

[25] M. Sanjose, S. Moreau, Numerical simulations of a low-speed radial fan, Int. J. Eng. Syst. Modell. Simul. 4 (2012) 47–58.

[26] A. Rynell, G. Efraimsson, M. Chevalier, M. Åbom, Inclusion of upstream turbulent inflow statistics to numerically acquire proper fan noise characteristics, SAE Tech. Pap. (2016), 2016-01-1811.

[27] A. Rynell, M. Chevalier, M. Åbom, G. Efraimsson, A numerical study of noise characteristics originating from a shrouded subsonic automotive fan, Appl. Acoust. 140 (2018) 110–121.

[28] B. Hu, H. OuYang, Y. Wu, G. Jin, X. Qiang, Z Du, Numerical prediction of the interaction noise radiated from axial fan, Appl. Acoust. 74 (2013) 544–552.

[29] H. Reese, T. Carolus, Axial fan noise: Towards sound prediction based on numerical unsteady flow data – a case study, J. Acoust. Soc. Am. 123 (2008) 4069–4074.

[30] R. Fitzpatrick, Chapter 1.6 in Theoretical Fluid Mechanics, IOP Publishing, London, 2017. Version: 20171201.

[31] J.H. Ferziger, M. Peric, Computational Methods for Fluid Dynamics, 3rd rev. ed., Springer-Verlag, Berlin, 2002.

[32] Siemens PLM Software. STAR-CCM+ User Guide (Version 12.04) 2017.

[33] H.-D. Yao andL. Davidsson, Vibro-acoustics response of simplified glass window excited by the turbulent wake of a quarter-spherocylinder body, J. Acoust. Soc. Am. 146 (2019) 3163–3176.

[34] M.L. Shur, P.R. Spalart, M.K. Strelets, A.K. Travin, A hybrid RANS-LES approach with delayed-DES and wall-modelled LES capabilities, Int. J. Heat Fluids Flow 29 (2008) 1638–1649.

[35] K.S. Brentner, F. Farassat, Analytical comparison of the acoustic analogy and Kirchhoff formulation for moving surfaces, AIAAA J. 36 (1998) 1379–1386.

[36] P. Spalart, S. Deck, M. Shur, K. Squires, M. Strelets, A. Travin, A new version of detached-eddy simulation, resistant to ambiguous grid densities, Theor. Comput. Fluid Dyn. 20 (2006) 181–195.

[37] W. Neise, Review of fan noise generation mechanisms and control methods, in: Proceedings of the Fan Noise 1992 International Symposium, Senlis, France, 1992, pp. 45–56.

[38] M. Younsi, F. Bakir, S. Kouidri, R. Rey, Numerical and experimental study of unsteady flow in a centrifugal fan, in: Proceedings of the 7th European Turbomachinery Conference, Athens, Greece, 2007, pp. 175–189, 2007.

[39] M. Branny, M. Karch, W. Wodziak, M. Jaszczur, R. Nowak, J.S. Szmyd, An experimental validation of a turbulence model for air flow in a mining chamber, J. Phys. Conf. Ser. 530 (2014), 012029.

[40] O. Baris, F. Mendonça, Automotive turbocharger compressor CFD and extension towards incorporating installation effects, in: Proceedings of the ASME Turbo Expo 2011: Power for Land, Sea and Air, 2011.

[41] H.-D. Yao, L. Davidson, L.E. Eriksson, Surface integral analogy approaches for predicting noise from 3D high-lift low-noise wings, Acta Mech. Sin 30 (2014) 326–338.

[42] M.S. Howe, Sound generated by fluid-structure interactions, Comput. Struct. 65 (1997) 433–446, https://doi.org/10.1016/S0045-7949(96)00259-3.